Synthesis and characterization of polybenzoxazine/clay hybrid nanocomposites for UV light shielding and anti-corrosion coatings on mild steel

Article *in* Journal of Polymer Research · August 2021

DOI: 10.1007/s10965-021-02657-0

CITATIONS
0

READS
37

6 authors, including:

Mohamed Gamal Mohamed Abuosoaud
National Sun Yat-sen University
102 PUBLICATIONS **1,210** CITATIONS
SEE PROFILE

Abdulsalam Mahdy
Assiut University
6 PUBLICATIONS **34** CITATIONS
SEE PROFILE

Rami J. Obaid
Umm Al-Qura University
25 PUBLICATIONS **69** CITATIONS
SEE PROFILE

Mohamed Hegazy
Egyptian Petroleum Research Institute (EPRI), Nasr City, Cairo, Egypt
80 PUBLICATIONS **2,778** CITATIONS
SEE PROFILE

Journal of Polymer Research (2021) 28:297
https://doi.org/10.1007/s10965-021-02657-0

ORIGINAL PAPER

Synthesis and characterization of polybenzoxazine/clay hybrid nanocomposites for UV light shielding and anti-corrosion coatings on mild steel

Mohamed Gamal Mohamed[1,2] · Abdulsalam Mahdy[1,3] · Rami J. Obaid[4] · Mohamed A. Hegazy[5] · Shiao-Wei Kuo[2] · Kamal I. Aly[1]

Received: 8 June 2021 / Accepted: 7 July 2021

Abstract

A novel benzoxazine (BA-BZ-COOH) monomer has been prepared and its structure has been proved using various measurements. PBA-BZ-COOH/nanocomposites reinforced with varying content of modified nanoclay (MNC) have been prepared in situ polymerization method for superior thermal, optical, and anti-corrosion properties. The resulting nanocomposites are showed a good dispersion of MNC in the PBA-BZ-COOH matrix without aggregates and a partial intercalated/exfoliated structure. The PBA-BZ-COOH/MNC (3%) composite that cured at 210 °C had high glass transition temperature (190 °C), and high UV shielding (97 and 85% at wavelength 275 and 375 nm, respectively). Finally, PBZs nanocomposites with varying contents of MNC (0.5, 1, 2, and 3%) were prepared as coatings on MS and their anti-corrosion performance were discussed in detail. The electrochemical results showed enhanced the polarization resistance of nanocomposites coatings with the increase of MNC content and the capacitance value for PBA-BZ-COOH/ MNC (3%) composite coating was reduced by about one orders of magnitude (0.00937 μF cm^2), compared with the neat PBA-BZ-COOH coating (0.01306 μF cm^2). Thus, PBA-BZ-COOH/MNC nanocomposites can be widely used for many industrial applications.

Keywords Ring-opening polymerization · Polybenzoxazine · Mild steel · Anti-corrosion behavior

Introduction

Benzoxazine monomers are heterocyclic precursors usually synthesized through Mannich condensation reaction of phenolic derivatives, aldehyde, and primary amines in the absence of any catalyst and either in solvent or solventless methods [1–12]. Their corresponding polybenzoxazines (PBZs) are one type of thermosetting polymers which frequently used in many potential applications because they have superior advantages, such as low dielectric constants, high thermal stability, near-zero polymerization shrinkage, high glass transition temperatures, low surface free energy, high carbon residue content, and superhydrophobic surfaces [13–27]. Nevertheless, PBZs have some disadvantages, such as a high curing temperature and difficulty in processing [20–25]. Ronda et al. prepared a series of benzoxazine monomers containing COOH and they found that the acid character of these reactive benzoxazine monomers led to an increase of the oxonium concentration, thus catalyzing the ROP of the oxazine rings [25]. UV radiation is one of the environmental factors which cause degradation for semiconductor devices, dyes, and pigments, so improved the UV resistance of materials for increasing their service lifespan has much attention in the ten last years. PBZs often have low UV shielding because of easily destroyed their backbone (Mannich Bridge) under UV radiation [28]. Kumar et al. developed the

✉ Mohamed Gamal Mohamed
mgamal.eldin12@yahoo.com

✉ Kamal I. Aly
kamalaly@aun.edu.eg

1 Polymer Research Laboratory, Chemistry Department, Faculty of Science, Assiut University, Assiut 71516, Egypt

2 Department of Materials and Optoelectronic Science, Center of Crystal Research, National Sun Yat-Sen University, Kaohsiung 804, Taiwan

3 Chemistry Department, Faculty of Education and Science, Rada'a Al-Baydha University, Al-Baydha 38018, Yemen, Saudi Arabia

4 Research Laboratories Unit, Faculty of Applied Science, Umm Al-Qura University, Makkah 21955, Saudi Arabia

5 Petrochemicals Department, Egyptian Petroleum Research Institute (EPRI), Nasr City, Cairo 11727, Egypt

Published online: 14 July 2021

UV shielding performance of PBZ using bio-silica, cardanol, and a new bis(quinoline amine) nanocomposite [29]. In general, the incorporation of nanocomposites into organic polymers could improve the properties of polymers (such as thermal stability, tensile stress, toughness, modulus, and corrosion, and UV resistance) [29–33]. Polymer/nanoclay composites have been the most important in academic and industry fields because of the good dispersion of clay particles in the polymer matrix and the controlling of clay-polymer interactions [34]. Additionally, nanoclay has been superior properties, such as a high capacity for cation exchange, low cost, easy modification of its surface and it could hinder the free motion of polymer chains [35]. Recently, our group reported that the addition of nanoclay (Na-bentonite) to PBZs coatings, their corrosion resistance properties on mild steel (MS) in a different corrosive media was enhanced which attributed to the good dispersion of silicate layers in the PBZ matrix [36, 37]. Furthermore, the improvement of thermal, mechanical, and anti-corrosion properties of PBZs was achieved by blending PBZ matrix with different materials including siloxane-polyimide (SPI), epoxy, polyurethane, and clay nanocomposites [38–43]. PBZs/inorganic hybrid nanocomposites have many potential applications including conductive coatings, mold releasing agents, packaging materials, green flame-retardants, low dielectric constant, adhesive layers, and microelectronic fabrication devices [44–46]. Laatar et al. revealed that unsaturated polyester reinforced with modified montmorillonite (UP/OMMT) nanocomposite coatings showed higher corrosion protection efficiency (96.84%) than that of the unmodified montmorillonite (UP/MMT) nanocomposite coatings (72.94%) on stainless steel in seawater media [47]. Herein, a novel benzoxazine monomer (BA-BZ-COOH) containing a catalytic COOH group was prepared through Mannich condensation of (1E,4E)-1,5-bis(4-hydroxyphenyl)penta-1,4-dien-3-one (BHBA), 4-aminobenzoic acid, and paraformaldehyde in 1,4-dioxane, as shown in Scheme 1. After that, the PBA-BZ-COOH/modified nanoclay (MNC) (0, 0.5, 1, and 3%) composites were prepared in situ polymerization method. The structure and properties of PBA-BZ-COOH/modified nanoclay (MNC) (0, 0.5, 1, and 3%) composites were investigated by FT-IR, TEM, SEM, XRD, DSC, TGA, and UV–Vis spectroscopy. Finally, the anti-corrosive behavior of PBA-BZ-COOH and PBA-BZ-COOH/MNC nanocomposites coatings on MS were evaluated using PDP and EIS in a 3.5% of NaCl solution.

Experimental

Materials

4-Aminobenzoic acid, paraformaldehyde $(CH_2O)_n$, 4-hydroxybenzaldehyde, boron trifluoride diethyl etherate ($BF_3O(C_2H_5)_2$) (37%), acetone (C_3H_6O), ethyl acetate (EA), methanol (CH_3OH), tetrahydrofuran (THF), 1,4-dioxane, sodium bicarbonate ($NaHCO_3$), and diethyl ether $(C_2H_5)_2O$ were obtained from Across Chemical Company and used as received. Hydrophilic nanoclay powder (Na-bentonite) and tetrabutylammonium iodide (TBAI) are obtained from Aldrich (Hamburg, Germany).

Preparation of (1E,4E)-1,5-bis(4-hydroxyphenyl) penta-1,4-dien-3-one (BHBA)

The BHBA was prepared according to a procedure reported elsewhere [48, 49]. Yield: 85%, T_m: 230 °C. ^{1}H-NMR (400 MHz, DMSO-d_6, δ, ppm, Fig. S1): 6.83, 7.63 (m, 8H, ArH), 7.03–7.68 (m, 4H, CH=CH), 10.00 (s, 2H, OH). FT-IR (KBr, cm^{-1}): 3325 (OH stretching), 1675.11 (C=O stretching), 1597 (C=C stretching). (+)ESI–MS m/z 266.15 (Calcd for $C_{17}H_{14}O_3$) (Fig. S2).

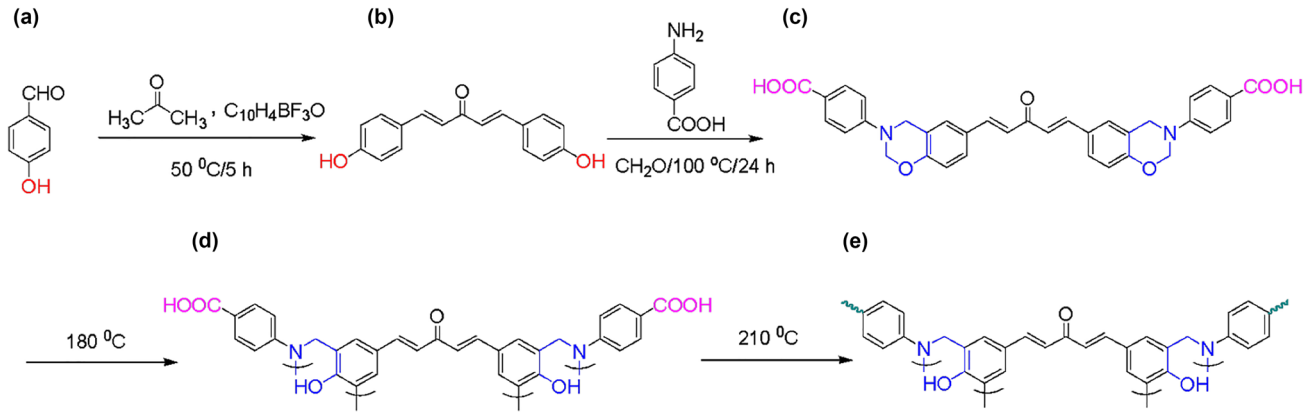

Scheme 1. Synthesis of (**b**) BHBA, (**c**) BA-BZ-COOH, (**d**) PBA-BZ-COOH, and (**e**) further crosslinking of PBA-BZ-COOH from (**a**) 4-hydroxybenzaldehyde

Preparation of 4,4′-(6,6′-((1E,4E)-3-oxopenta-1,4-diene-1,5-diyl) bis(2H-benzo[e][1,3]oxazine-6,3(4H)-diyl))dibenzoic acid (BA-BZ-COOH)

A solution of 4-aminobnzoic acid (2.10 g, 0.015 mol), paraformaldehyde (0.90 g, 0.030 mol) in 1,4-dioxane (50 mL) was stirred under reflux at 80 °C for 30 min. Then, the BHBA (2.00 g, 0.008 mol) was added with continuous stirring. After 1 h, 4,4',4''-(1,3,5-triazinane-1,3,5-triyl) tribenzoic acid (intermediate of the reaction) was formed (Fig. S3). To overcome the formed triazine, the reaction temperature was raised to 100 °C and then the reaction was monitored by thin-layer chromatography (1:1, v/v EtOAc/hexane) until the reactants were disappeared completely. After that, 1,4-dioxane was evaporated by a rotary evaporator and the solid residue was dissolved in EA (100 mL) and washed three times with $NaHCO_3$ solution (5%), followed by water. The organic layer was dried over anhydrous $MgSO_4$, and the solvent was removed by a rotatory evaporator to afford a yellow powder. Yield: 60%. ^{1}H-NMR (400 MHz, DMSO-d_6, δ, ppm): 5.60 (s, 4H, O-CH_2-N), 4.80 (s, 4H, Ph-CH_2-N), 6.80–7.88 (m, 14H, ArH), 7.03, 7.82 (s, d, 4H, CH = CH), 12.20 (s, 2H, COOH). ^{13}C-NMR (400 MHz, DMSO-d_6, δ, ppm), 48.17 (ph-CH_2-N), 78.41 (O-CH_2-N), 188.51 (C = O), 162.12 (COOH), 188.51 (C = O. FT-IR (KBr, cm^{-1}): 1705.08 (C = O), 1601.79 (C = C), 1235.00 (C–O–C), 925.00 (oxazine ring). (+)ESI–MS m/z 591.41 (Calcd for $C_{35}H_{28}N_2O_7$) (Fig. S4).

Preparation of modified nanoclay (MNC)

The MNC was prepared via a cation exchange reaction between sodium cations of nanoclay and tetrabutylammonium iodide (TBAI) as organic ammonium salt (Organo-modifying agent) in distilled water, according to the procedure reported elsewhere [49]. A suspension of nanoclay (5.00 g) in distilled water (250 mL) was heated under stirring at 80 °C for 1 h. Subsequently, a solution of TBAI (2.50 g) and HCl (2.50 g) in distilled water (200 ml) was heated at 80 °C for 1 h and then was added into the nanoclay suspension with continuous stirring at the same condition for 3 h. The resulting precipitate was collected by vacuum filtration and suspended in hot distilled water with stirring for 1 h and filtered off. The solid residue was washed several times with an aqueous solution of $AgNO_3$ (1.0 mol) to remove all the halide ions and further twice with ethanol and dried at 80 °C for 12 h.

Preparation of PBA-BZ-COOH and its nanocomposites

The PBA-BZ-COOH/MNC composites with various weight percentages of MNC were prepared in-situ polymerization method; for example, 3 wt% of MNC in PBA-BZ-COOH/MNC composite was prepared as follows: 0.015 g of MNC was first dispersed in THF (20 mL) under the stirring at 80 °C for 2 h. Then, 0.49 g of BA-BZ-COOH monomer was added to MNC suspension with stirring at the same temperature for 3 h. The composite mixture was applied on a stainless-steel plate as a film by spin coating and dried in an oven at 60 °C for 12 h. The resulting film was cured at 180 °C for 2 h and was cooled to room temperature. The same method was also used to prepare the PBA-BZ-COOH/MNC (0.5%) and PBA-BZ-COOH/MNC (1%) composites.

Preparation of the PBA-BZ-COOH and its nanocomposite coatings for corrosion tests

The mild steel (MS) specimens (composition, weight %: 0.19% C, 0.94% Mn, 0.05% Si, 0.022% Cu, 0.009% P, 0.004% S, 0.014% Ni, 0.034% Al, 0.009% Cr, 0.016% V, 0.003% Ti and Fe remainder) were provided by the Egyptian Petroleum Research Institute, Cairo, Egypt. Its surface was polished with sandpaper and washed with distilled water, followed by acetone, and dried. A solution of BA-BZ-COOH monomer and the varying content of MNC (0, 0.5, 1, 2, and 3%) in THF (100 g L^{-1}) were sonicated separately for 30 min until a homogeneous solution was obtained. Then, the MS was dipped repeatedly into the prepared solution to obtain a uniform film thickness (about 5 µm) for all the samples and then dried in air overnight and lastly cured in an oven at 210 °C for 2 h, as presented in Fig. S5.

Results and discussion

Preparation of BA-BZ-COOH

A novel benzoxazine monomer, BA-BZ-COOH has been synthesized via Mannich condensation reaction of BHBA, 4-aminobenzoic acid, and paraformaldehyde in the 1,4-dioxane, as shown in Scheme 1. The chemical structure of the BA-BZ-COOH was confirmed by different analyses. The ^{1}H-NMR spectrum of BA-BZ-COOH (Fig. 1a) features two sharp signals at 5.60 and 4.80 ppm, representing N-CH_2-O and Ar-CH_2-N, respectively in its oxazine ring and the signals observed in the range 6.80–7.88 ppm; typically ascribed to aromatic protons [50]. The characteristics signals for the CH=CH unit and COOH groups appeared at 7.03 and 12.20 ppm, respectively. The ^{13}C-NMR spectrum of BA-BZ-COOH (Fig. 1b) characteristics two signals at 78.41 and 48.71 ppm, representing N-CH_2-O and Ar-CH_2-N, respectively in its oxazine ring. The resonance signals for C=O and COOH groups appeared at 188.51 and 167.12 ppm, respectively. in addition, carbon signals centered at 123.22 and 142.35 ppm which attributed to the presence of CH=CH unit [48].

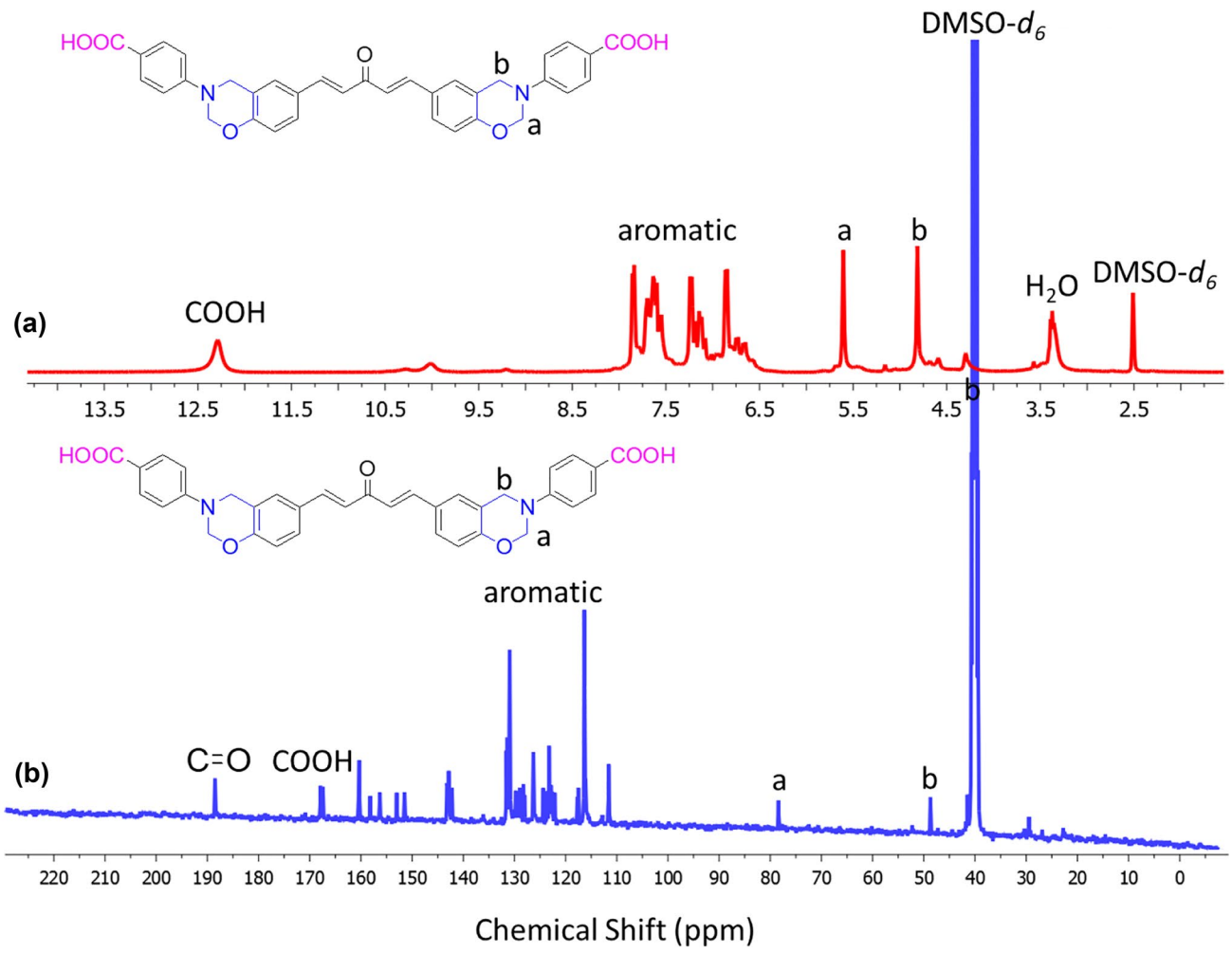

Fig. 1. ^{1}H and ^{13}C NMR of BA-BZ-COOH in DMSO-d_6, recorded at room temperature

Figure 2 represents the FTIR spectra of BHBA, BA-BZ-COOH, and PBA-BZ-COOH, recorded at 25 ^{0}C. The FT-IR spectrum of BHBA (Fig. 2a) featured absorption bands at 3325 and 1669 cm^{-1}, representing to the stretching OH and C = O units, respectively. The FT-IR spectrum of BA-BZ-COOH (Fig. 2b) features major absorption bands at 925 and 1235 cm^{-1} representing the oxazine ring, and C–O–C stretching. Also, the absorption bands centered at 3500–2928.90 cm^{-1} representing the hydrogen-bonded COOH dimer and free OH group [20]. The strong band centered at 1705.05 cm^{-1} attributed to the carbonyl (C = O) group. As expected, after thermal curing of the BZ precursor at 210 °C, the absorption bands of the oxazine ring completely disappeared and form PBA-BZ-COOH, as shown in Fig. 2c.

Figure 3 represents the UV–Vis absorption spectrum of BA-BZ-COOH in THF solution (6×10^{-4} M), after irradiation at 365 nm for various times. As shown in Fig. 3, two absorption peaks have appeared at 355 and 290 nm, which representing $\pi - \pi^*$ transition of C = C bisbenzylidene moiety and $\delta - \delta^*$ transition of cyclobutane ring, respectively. After each irradiation time, the intensity at 355 nm decreases while the intensity at 290 nm increases was

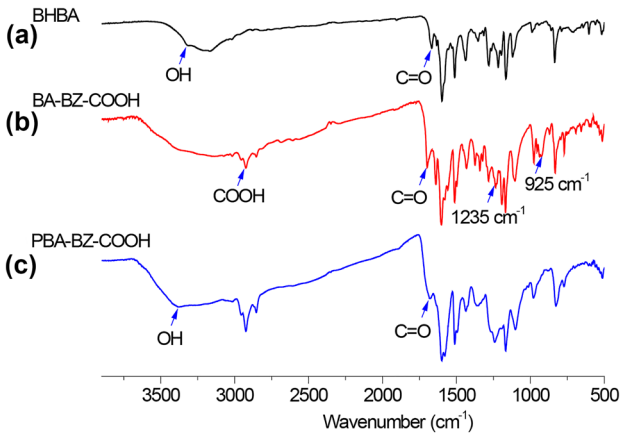

Fig. 2 FTIR spectra of (**a**) BHBA, (**b**) BA-BZ-COOH, and (**c**) PBA-BZ-COOH, recorded at 25 °C

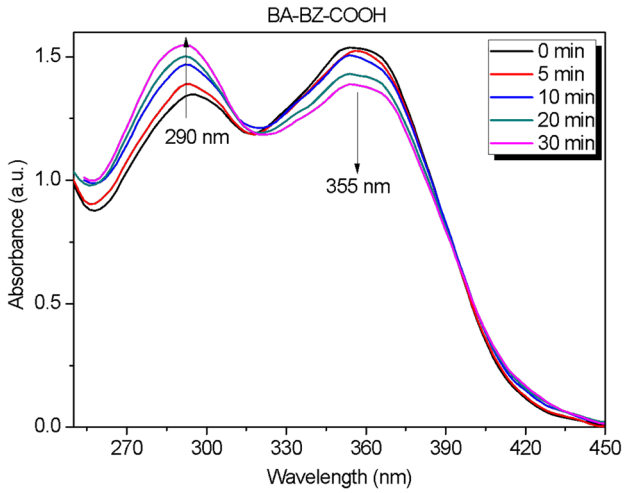

Fig. 3 UV–Vis absorption spectrum of the BA-BZ-COOH in THF solution

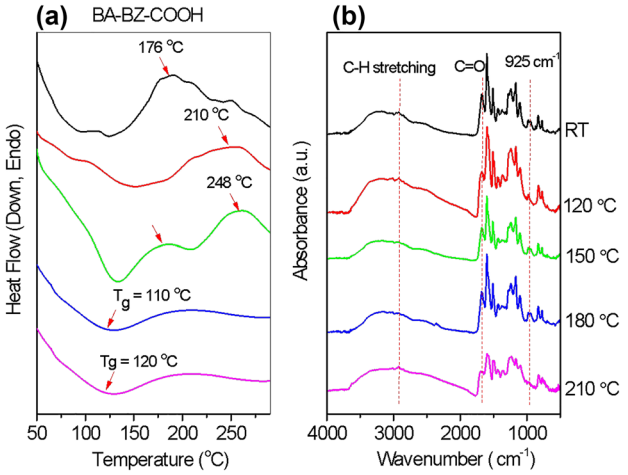

Fig. 4 (**a**) DSC and (**b**) FTIR analyses of BA-BZ-COOH before and after thermal treatments

observed. This behavior strongly indicated that the BA-BZ-COOH has photoreactive moiety (bisbenzylidene), which can be undergone to a photodimerization reaction when its exposure to light irradiation. All the above results suggesting a successful synthesis of the BA-BZ-COOH.

Thermal ring-opening polymerization behavior of the BA-BZ-COOH

We used DSC and FT-IR analyses to study the polymerization behavior of the neat BA-BZ-COOH and its nanocomposites. The DSC thermograms of the neat BA-BZ-COOH after various curing stages (Fig. 4a) featured a broad exothermic peak with an onset of about 160 °C and maximum at 176 °C for the uncuring BA-BZ-COOH monomer. A broad exothermic peak is due to that the curing reaction of the oxazine ring is partially overlapped with the endothermic peak (decarboxylation reaction) at about 220 °C [51]. The lowering of the polymerization reaction peak for the BA-BZ-COOH at 176 °C, can be attributed to the catalytic effect of the carboxylic acid groups compared with other benzoxazines [52, 53]. After curing at 180 °C, this exothermic peak disappeared, which confirms the complete curing reaction of the benzoxazine precursor. The polymerization behavior of the BA-BZ-COOH was further studied by FT-IR spectra, as shown in Fig. 4b. From this Figure, after each curing stage, the intensity absorption bands of benzoxazine monomer (925, 1110, and 1235 cm^{-1}) [51] gradually decreased and when the curing temperature was 180 °C, they are completely disappeared, indicating that the completion of the curing reaction at this temperature. Furthermore, the broad peak at about 3300 cm^{-1} was appeared due to intermolecular hydrogen bonding of phenolic–OH resulted from the opening of the oxazine ring. Finally the absorption band of the COOH group at 1705.08 cm^{-1} gradually decreased after thermal treatments at 180 and 210 °C, suggesting that the curing reaction of our new benzoxazine was done with partial decarboxylation of the COOH group [53]. The photoluminescence (PL) behavior of the BA-BZ-COOH was studied at various concentrations in THF, as shown in Fig. 5a. The PL intensity of the BA-BZ-COOH at 450 nm gradually increases when the concentration increased from 10^{-6} to 10^{-2} M. The increase of the blue fluorescence intensity band at 450 nm can be ascribed to the formation of aggregates from [54]. This AIE phenomenon of the BA-BZ-COOH was also confirmed by measuring the emission property of the BA-BZ-COOH monomer in H_2O/THF mixtures at 365 nm, as shown in Fig. 5b. It was observed that the BA-BZ-COOH in pure THF solution gave a weak emission and when the water fraction increases from 0 to 90%, the emission intensity at 520 nm increased due to the solution aggregate and restriction of intramolecular motion through a space conjugation [55].

The effect of curing temperatures on the thermal stability of the BA-BZ-COOH was studied using TGA analysis, as shown in Fig. 6, recorded under N_2 atmosphere from 25 to 800 °C and their results are summarized in Table S1. In general, the TGA profile of the BA-BZ-COOH showed three main degradation steps; the initial step including drain of adsorbed water molecules and degradation of carboxyl group which was occurred in the temperature below 200 °C [20]. The second step can be observed in the temperature range 250 to 350 °C, due to the cleavage of the Mannich bridge [52]. Finally, the release of phenols and degradation of aromatic rings in the polymer chain occurred between 350 to 600 °C. It is seen from Fig. 6 and Table S1, the decomposition temperatures at 5 and 10 wt% and the char yield for the BA-BZ-COOH increase with the increase of the curing temperatures. After curing at 210 °C, the T_{d5}, $T_{d10,}$ and char

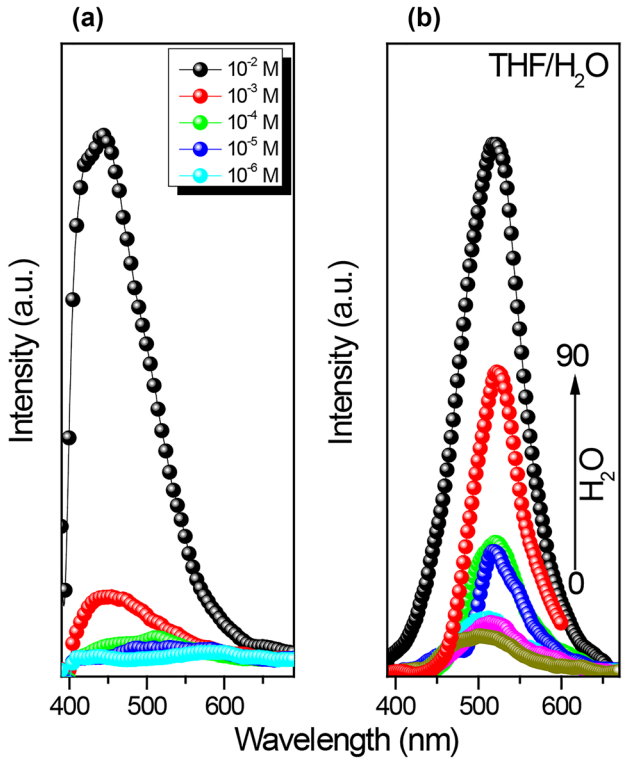

Fig. 5 Photoluminescence analyses of the BA-BZ-COOH at different THF concentrations (**a**) and with different water contents (**b**)

yield values of BA-BZ-COOH increased due to an increase in the cross-linkages resulted further from the decarboxylation process of the COOH group at this temperature. The thermal stability values for the BA-BZ-COOH, after curing at 210 °C are much higher than those BzFA and BzPFA [53]. The limiting oxygen index (LOI) values of the uncuring

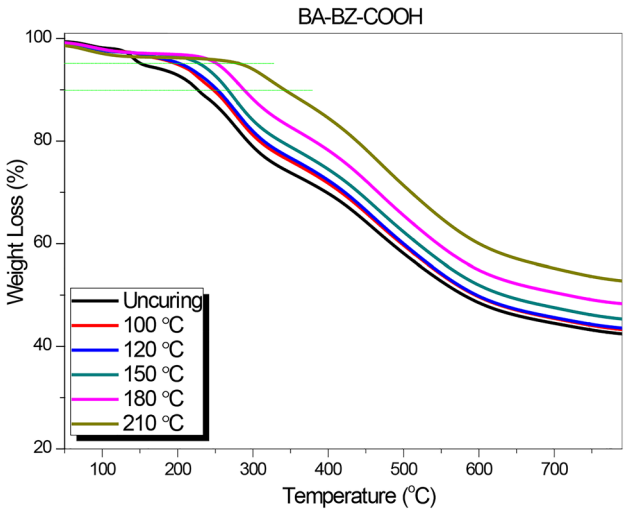

Fig. 6 TGA analyses of the BA-BZ-COOH before and after thermal treatments

BA-BZ-COOH and after different curing stages (Table S1) are theoretically calculated using the char yield values, by the following Van Krevelen and Hoftyzer equation [56].

$$LOI = 17.5 + 0.4\ CY$$

where CY is the percentage of the char yield at 800 °C, and the LOI values for PBA-BZ-COOH were > 38, indicates that our PBZ materials possess high flame retardancy property, which can be effectively used as non-phosphorus and non-halogen flame retardant materials for various industrial and engineering applications in the form of sealants, encapsulants, and coatings [36].

Characterization of organomodified nanoclay (MNC) and characterization of PBA-BZ-COOH/MNC nanocomposites

The modification of nanoclay aims to enhance its dispersibility and compatibility with a polymer chain by an ionic exchangeable agent. Herein, we have modified the nanoclay (Na- bentonite) using TBAI as ammonium salt in distilled water (Scheme 2)**.**

The XRD patterns of unmodified nanoclay and MNC showed in Fig. 7A, which were performed from 4 to 40°. Interestingly, the broad diffraction peak of unmodified nanoclay was observed at 2θ=6.16° and d-spacing of 14.348 °A (Fig. 7A(a)). Then after its modification, this diffraction peak of MNC shifted to a smaller angle at 6.28° and d-spacing was increased to 14.074 °A (Fig. 7A(b)), due to the intercalated of alkylammonium cations into the clay layers [57]. The structures of unmodified nanoclay and MNC were also examined by FT-IR spectra, as shown in Fig. 7B. Figure 7B (a) showed the FTIR spectrum of the unmodified nanoclay which features the appearance of the bands at 3451 and 1642 cm^{-1}, corresponding to O–H stretching and bending, respectively, and the bands at 1042 and 523 cm^{-1} are characteristics to Si–O and Si–O-Al stretching in unmodified nanoclay, respectively. On the other hand, the FT-IR spectrum of MNC (Fig. 7B(b)) features three new absorption bands at 2876, 2964, and 1384 cm^{-1}, attributed to $-CH_2$, $-CH_3$, and C-N, respectively in the modifying agent, compared with the unmodified nanoclay [58], indicating that the TBAI was strongly intercalated into the silicate layers in the unmodified nanoclay. The PBA-BZ-COOH/MNC (0.5, 1, and 3%) composites were prepared in-situ polymerization process, which is based on intercalation of a monomer inside the silicate layers in THF and thermal ROP, as shown in Scheme 2. In the XRD pattern of PBA-BZ-COOH/MNC (3%) composite (Fig. 7A(c)), we observed that the diffraction peak shifted to be 6.7° and interlayer spacing is significantly increased to be 13.193 °A compared with the unmodified nanoclay and MNC, suggesting that the polymer intercalated the MNC. It was also found that a weak intensity peak at 6.16° was

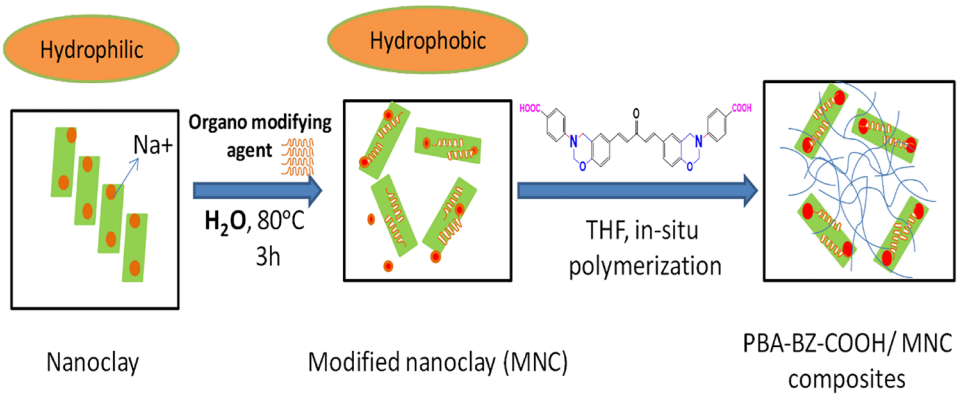

Scheme 2. Schematic cartoon for the preparation of modified nanoclay and PBA-BZ-COOH/ MNC composites

remained in the PBA-BZ-COOH/MNC (3%) composite, indicating that a partially exfoliated nanocomposite structure was obtained, which is in good consistent with the previous reported [49]. Furthermore, the new absorption peak appeared at 1042 cm^{-1} in the FTIR spectrum of the PBA-BZ-COOH/MNC (3%) composite, due to the Si–O stretching of silicate layers, suggesting that the polymer intercalated in between the silicate layers in the MNC.

Figure 8(a) displays DSC thermograms of the BA-BZ-COOH/MNC (3%) composite before and after different curing stages. It can be observed that the exothermic peak for the uncuring BA-BZ-COOH/MNC (3%) composite significantly shifted into lower curing temperature (135 °C) compared with the neat BA-BZ-COOH (176 °C) in this study and is much lower than that of TPEP-BZ/SWCNT nanocomposites (262 °C) [59]. This due to the presence of the catalytic effect of carboxylic acid groups and an onium ion in the MNC surface [49]. The two endothermic peaks were also observed at 190, and 240 °C, which are corresponding to the decarboxylation reaction and evaporation of water molecules in the MNC, respectively. However, the exothermic peak and endothermic peak were disappeared gradually with the increase of the curing temperature. After curing at 180 °C, the exothermic peak is completely disappeared, indicating that the ring-opening polymerization of the oxazine unit in nanocomposites was done at this temperature. Similarly, this behavior was also confirmed by FT-IR analyses (Fig. 8b). These results imply that the COOH groups and the MNC molecules are accelerating the polymerization reaction of benzoxazine in the resulting nanocomposites to lower temperatures. Also, after curing at 210 °C, the resulting PBA-BZ-COOH/MNC (3%) nanocomposites exhibited higher glass transition temperature (T_g) (190 °C) than that of the PBA-BZ-COOH (120 °C) as showed in the DSC thermograms (Fig. 4a). The increase in the T_g value of PBA-BZ-COOH/MNC(3%) composite is because that the MNC with the alkyl side chain acts as a stiffening agent and restricted motion of the polymeric chains [60].

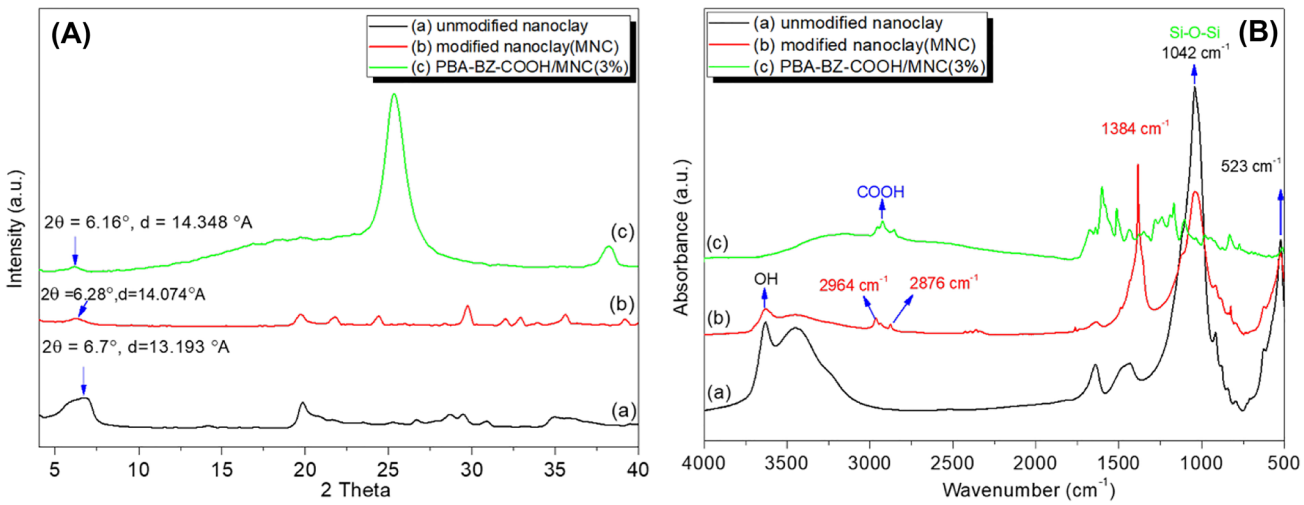

Fig. 7 (**A**) XRD profiles of (**a**) unmodified nanoclay, (**b**) unmodified nanoclay (MNC), and PBA-BZ-COOH/MNC (3%). (**B**) FTIR spectra of (**a**) unmodified nanoclay, (**b**) unmodified nanoclay (MNC), and PBA-BZ-COOH/MNC (3%).

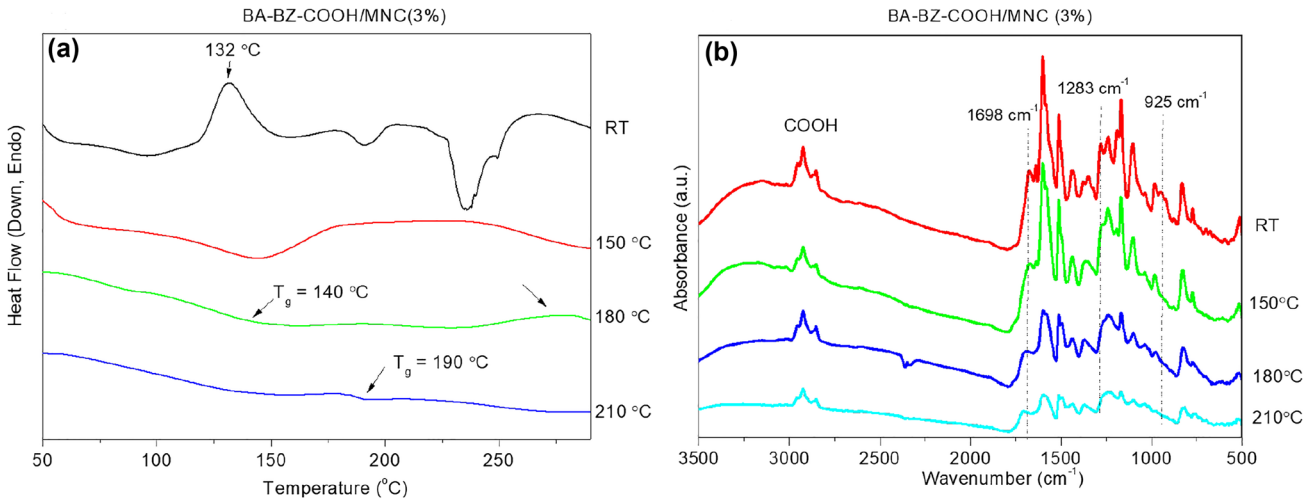

Fig. 8 (**a**) DSC and (**b**) FTIR analyses of PBA-BZ-COOH/MNC (3%) nanocomposites before and after thermal treatments

The dispersion of the modified nanoclay (MNC) in the resulting PBA-BZ-COOH was investigated by transmission electron microscopy (TEM). Figure 9 displays the TEM images of PBA-BZ-COOH /MNC (3%) composites. It can be seen the uniform platelets and intercalated tactoids of the same thicknesses were achieved in the resulting nanocomposites with MNC. In addition, the presence of a few stacks and bundles can be attributed to the Van der Waals interactions between the MNC layers. The hair-like structures without aggregates can be also observed for nanocomposites with MNC, due to enhancing the interfacial interactions between MNC and PBA-BZ-COOH matrix [61].

The surface morphologies of the neat PBA-BZ-COOH and its nanocomposites with varying content of MNC are also investigated by SEM images as shown in Fig. 10. SEM images of the neat PBA-BZ-COOH showed the surface is flat and very smooth, suggesting a hydrophilic surface (Fig. 10a). The SEM image of PBA-BZ-COOH/MNC (0.5%) composite (Fig. 10b) showed the surface is rough, and the existence of some small particles on the surface. However, the number of the small particles and rougher surfaces of nanocomposites increased with the increasing of the MNC contents. Furthermore, a homogeneous dispersion of MNC particles in the PBA-BZ-COOH matrix was achieved for PBA-BZ-COOH/MNC (3%) composite (Fig. 10c and d), which ascribed to the stronger interaction between PBA-BZ-COOH chains and the MNC surface.

Optical properties of the PBA-BZ-COOH and its nanocomposites

Figure 11a shows the UV–Vis absorption spectra of the neat PBA-BZ-COOH and its nanocomposites with various contents of MNC (0.5, 1, and 3 wt %) in THF (6×10^{-4} M). The UV–Vis absorption spectrum of the neat PBA-BZ-COOH featured an absorption peak maximum at 332 which due to π-π* transition in bisbenzylidene moiety. The absorption intensity of PBA-BZ-COOH is gradually reduced as the MNC content increase in the nanocomposites. This suggests that the compatibility and effective chemical interactions between MNC

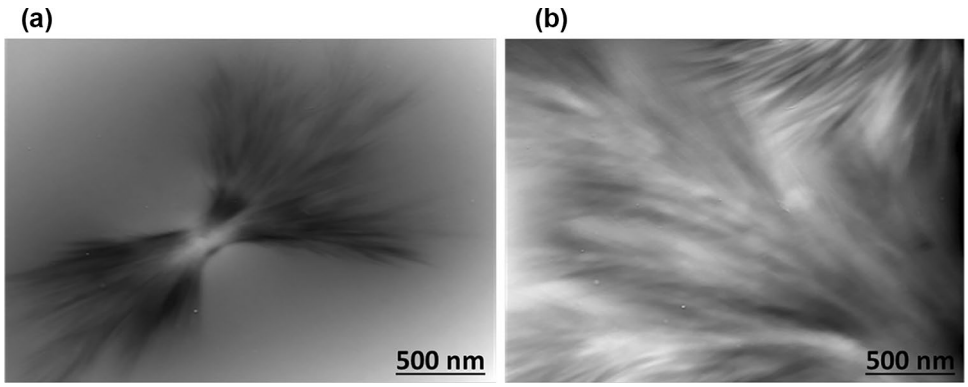

Fig. 9 TEM images of the PBA-BZ-COOH/MNC (3%) composites

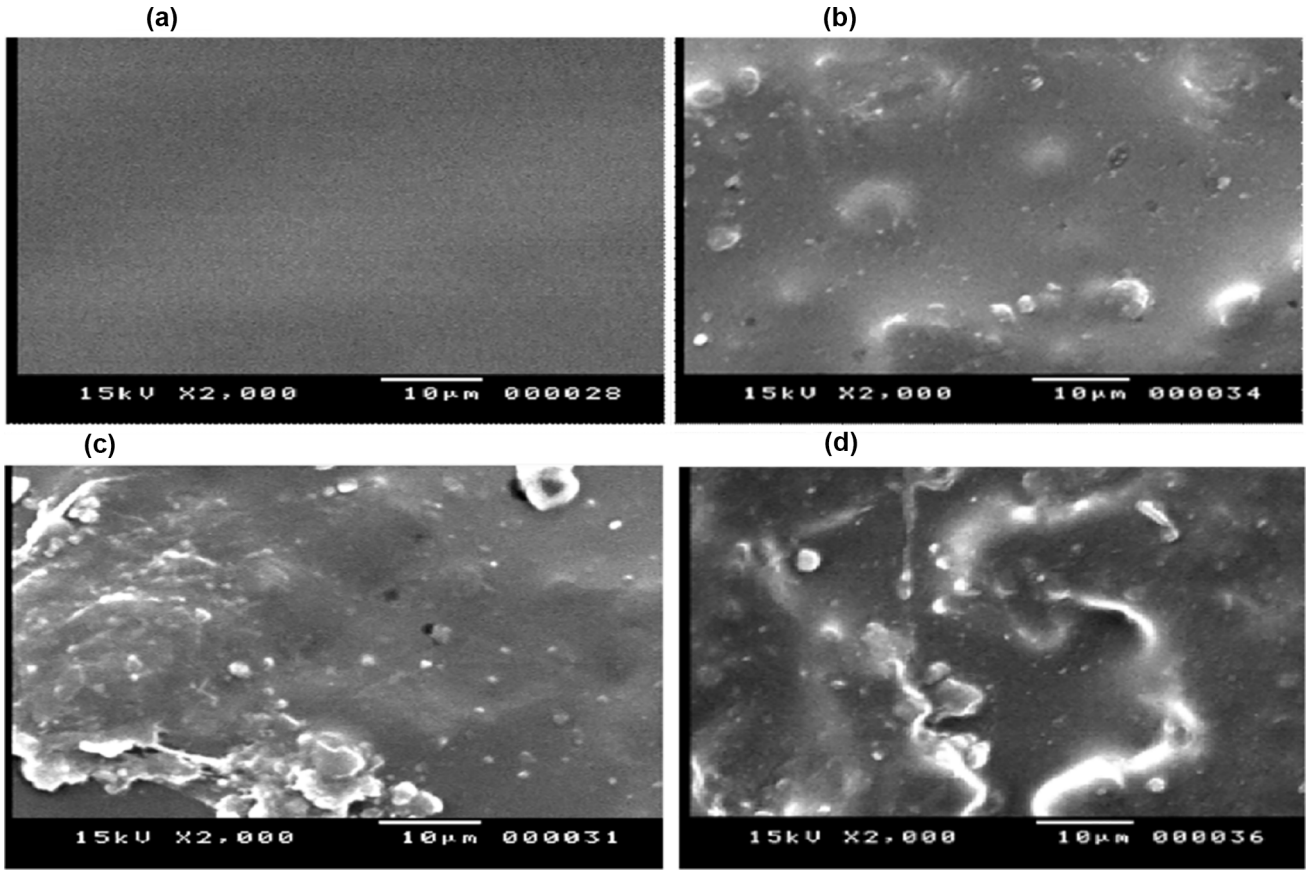

Fig. 10 SEM images of (**a**) PBA-BZ-COOH, (**b**) PBA-BZ-COOH/MNC (0.5%), and (**c**, **d**) PBA-BZ-COOH/MNC (3%)

and PBA-BZ-COOH matrix. Thus, these nanocomposites can be used as effective UV protection coatings. The UV shielding behaviors of the neat PBA-BZ-COOH and its nanocomposites were investigated using UV–Vis spectroscopy, recorded as transmittance spectra (Fig. 11b). From this Figure, it can be observed that the UV shielding behavior of the nanocomposites enhanced with the increase of the MNC content compared with the neat PBA-BZ-COOH. The PBA-BZ-COOH/MNC (3%) composite showed a higher UV shielding behavior about of 97 and 85% at the wavelength of 275 and 375 nm: respectively. Whereas the neat PBA-BZ-COOH showed only 80 and 50% of UV shielding radiation at the same conditions. Therefore, the enhancement of UV shielding performance of the nanocomposite films can be attributed to a uniform dispersion of MNC in the PBA-BZ-COOH matrix and the formation of strong interfacial bonding between the MNC and PBA-BZ-COOH matrix.

Anti-corrosive behaviors of the PBA-BZ-COOH and its nanocomposite coatings

The Potentiodynamic polarization (PDP) measurements (Tafel curve) have been used to examine anti-corrosion behaviors of the neat PBA-BZ-COOH and its nanocomposites coatings with various content of modified nanoclay (MNC) on MS in 3.5% NaCl solution at ambient

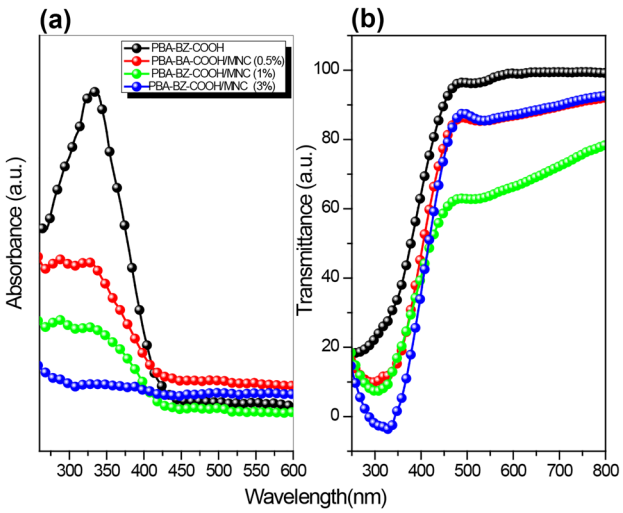

Fig. 11 (**a**) UV–Vis absorption and (**b**) UV–vis light transmittance spectra of neat PBA-BZ-COOH and its nanocomposites

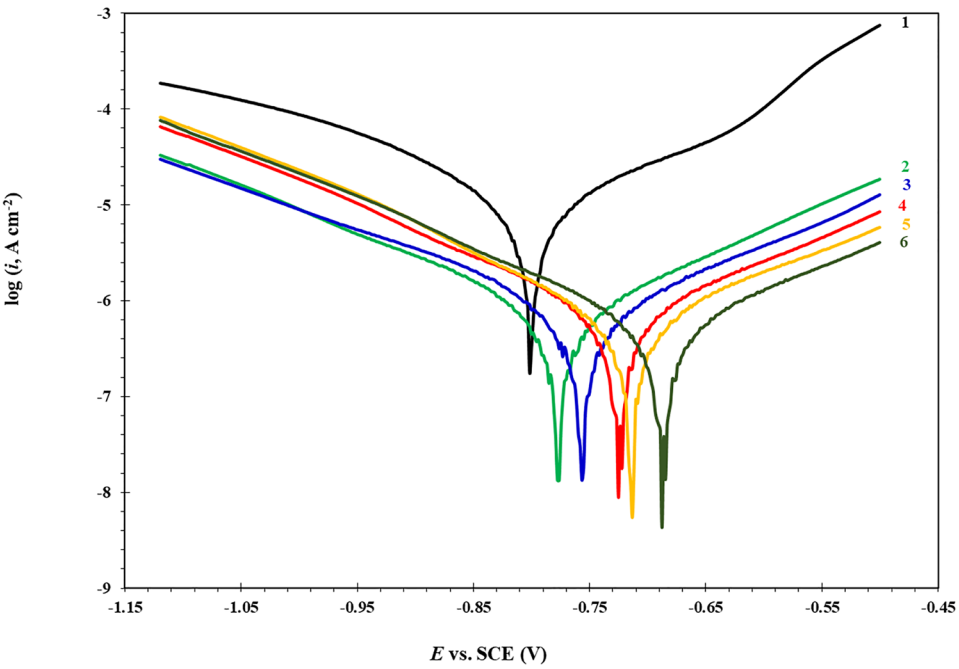

Fig. 12 Tafel plots of uncoated MS (1) and MS coated with PBA-BZ-COOH (2), PBA-BZ-COOH/MNC (0.5%) (3), PBA-BZ-COOH/MNC (1%) (4) PBA-BZ-COOH/MNC (2%) (5), and PBA-BZ-COOH/MNC (3%) (6) in 3.5 wt.% NaCl

temperature, as shown in Fig. 12. The corrosion current densities (i_{corr}), corrosion potential (E_{corr}), anodic Tafel slope (β_a) and cathodic slope (β_c) parameters for all the tested samples were determined by volt master 4 software [62] for the cathodic and anodic curves. The corrosion rate (*CR*) and the corrosion protection efficiency (η) values of the samples are calculated using Eqs. (1) and (2), respectively, based on the i_{corr} densities values [54, 63, 64].

$$CR = \frac{EW \times k \times i_{corr}}{A\rho} \quad (1)$$

where EW is the equivalent weight of the MS (g eq^{-1}), k is the CR constant (3272 mm $year^{-1}$), i_{corr} is the corrosion current density (μA cm^{-2}), A is the electrode area (cm^2), and ρ is the MS density (g cm^{-3}).

$$\eta = \frac{i_{corr} - i_{corr(c)}}{i_{corr}} \times 100 \quad (2)$$

where i_{corr} and i_{corr} (c) are the corrosion current densities for the bare MS and coated MS, respectively.

All the obtained PDP parameters are summarized in Table 1. As shown in Fig. 12 and Table 1, after MS coated with PBA-BZ-COOH precursors, all the anodic and the cathodic currents significantly reduced, indicating hinders the anodic dissolution and prevent the penetration of corrosive ions (water and chloride ions) and access to MS surface, due to the barrier effect of the composite's coatings [47, 65]. The anti-corrosion performances of the nanocomposite coatings enhanced as their MNC content were an increase, due to the increased resistance of the nanocomposite coatings to the diffusion of the corrosive ions [66, 67]. The *CR* value of the PBA-BZ-COOH/MNC (3%) composite coating was (4.848 μm Y^{-1}), this value lower by 3 times (11.120 μm Y^{-1}) and 30 times (145.40 μm Y^{-1}) compared with that of the neat PBA-BZ-COOH coating and the bare MS, respectively. the PBA-BZ-COOH/MNC (3%) coatings reduced the CR of

Table 1 Potentiodynamic polarization data of uncoated MS and MS coated with PBA-BZ-COOH, PBA-BZ-COOH/MNC (0.5%), PBA-BZ-COOH/MNC (1%), PBA-BZ-COOH/MNC (2%), and PBA-BZ-COOH/MNC (3%)

Coating Samples	E_{corr} (mV vs. SCE)	i_{corr} (μA cm^{-2})	β_a (mV dec^{-1})	β_c (mV dec^{-1})	CR (μm Y^{-1})	R_P (kΩ cm^2)	η (%)
Bare MS	-803.0	12.4395	281.9	-228.2	145.40	3.68	-
PBA-BZ-COOH	-777.5	0.9511	254.7	-222.9	11.12	50.06	92.35
PBA-BZ-COOH/MNC (0.5%)	-756.5	0.7796	247.7	-214.9	9.118	53.44	93.73
PBA-BZ-COOH/MNC (1%)	-714.5	0.5389	248.5	-216.1	6.302	77.37	95.67
PBA-BZ-COOH/MNC (2%)	-713.0	0.4803	247.0	-204.8	5.618	93.25	96.14
PBA-BZ-COOH/MNC (3%)	-687.5	0.4146	248.5	-206.1	4.848	110.35	96.67

MS much better than 3% nanoclay content and 20% epoxy resin/poly(CP-BZ).

nanocomposite coating (8.21 μm Y^{-1}) [37]. Moreover, E_{corr} for MS coated with nanocomposites gradually shifted towards the more positive potential with the increase of the MNC content, compared with bare MS, indicating that the nanocomposites coatings had surface passivation and protection efficiency reaching a maximum of 96.67%. Furthermore, the R_p of PBA-BZ-COOH/MNC (3%) composite coating was 110.35 kΩ cm^2, increasing of almost of 2 times was observed compared with that of the neat PBA-BZ-COOH (50.06 kΩ cm^2), and with that of 5% content of modified nanoclay polystyrene nanocomposites (CPS-AC5) [68]. This superior anti-corrosion behavior of our nanocomposite coatings can be attributed to the presence of the MNC barrier effect and a long π-electron conjugation of a polymer matrix, which caused a greater coverage for the MS surface. Also, the slopes of the anodic Tafel (β_a) and cathodic Tafel (β_b) lines are independent of nanocomposites as in Table 1. Where, anodic, and cathodic Tafel lines in the presence of nanocomposites often parallel to their counterparts for the MS bare. The anti-corrosive behaviors of the neat PBA-BZ-COOH and its nanocomposites with various content of modified nanoclay (MNC) are further evaluated using EIS measurements in 3.5 wt% NaCl solutions at ambient temperature. The Nyquist plots for the bare MS and the coated MS are presented in Fig. 13. From this figure, the same shapes for all curves were observed, but with different diameters, suggesting a similar anti-corrosive mechanism. The low-frequency loops showed that there is no ideal semi-circle, which was detected according to the EIS theory. This behavior can be attributed to the non-ideal performance of the double layers as a capacitor, because of the frequency dispersion, which is generally related to roughness and the heterogeneity of the MS surface [69]. The capacitive loop diameters of the nanocomposite's coatings increased with an increase in their MNC content, indicating that the charge transfer resistance increases and enhancement in anti-corrosive performance on MS surfaces.

We used an equivalent electric circuit model to be fitting of all the EIS data as shown in Fig. 14, which is typically simulated for the bare MS and coated MS electrodes, where Rs is the solution resistance (working electrode/reference electrode interface); R_{ct} and *CPE* is the charge transfer resistance and the coatings capacitance (working electrode/electrolyte interface), respectively. As is known, the R_s values do not technically or theoretically important in the analysis of the coating performance [70]. Herein, we replaced the capacitance of the coating samples with the constant phase element (CPE) to obtain a better fit for the experimental data [71]. In this study, EIS parameters were fitted using the ZSimpWin program and the results are tabulated in Table 2, the impedance of CPE was evaluated by Eq. (4) [72, 73]

$$Z_{CPE} = \frac{1}{Y_0(j\omega)^n} \tag{4}$$

where Y_o is the *CPE* magnitude, (n) is the phase shift, j is the imaginary unit, ω is the angular frequency ($\omega = 2\pi f_{max}$), where f is the coatings frequency.

The double-layer capacitance parameters (C_{dl}) of all the coatings were calculated from *CPE* values by Eq. (5) [74].

$$C_{dl} = Y_{\circ}(\omega_{max})^{n-1} \tag{5}$$

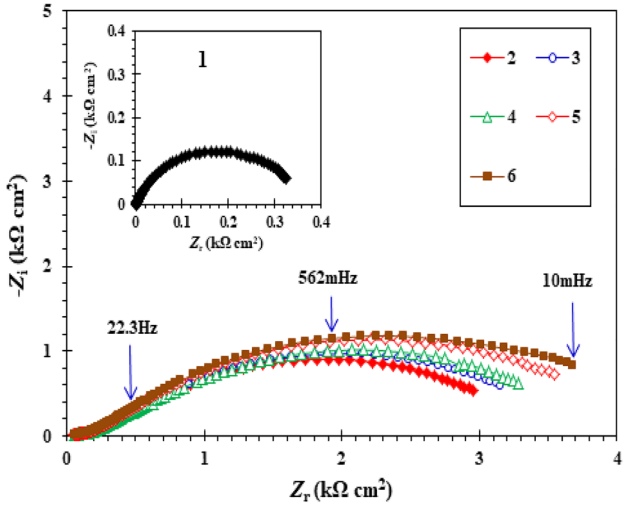

Fig. 13 Nyquist plots of uncoated MS (1) and MS coated with PBA-BZ-COOH (2), PBA-BZ-COOH/MNC (0.5%) (3), PBA-BZ-COOH/MNC (1%) (4), PBA-BZ-COOH/MNC (2%) (5), and PBA-BZ-COOH/MNC (3%) (6) in 3.5 wt.% NaCl

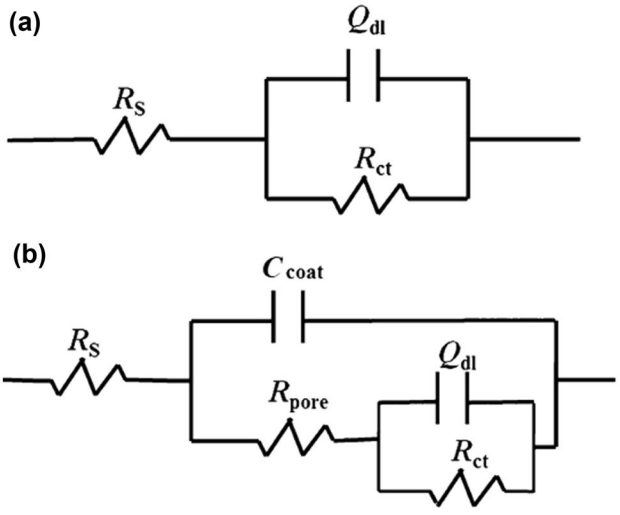

Fig. 14 The equivalent electrical circuit for the EIS data of the MS bare (**a**) and MS coating (**b**) in 3.5 wt% NaCl solution

Table 2 EIS data of uncoated MS and MS coated with PBA-BZ-COOH, PBA-BZ-COOH/MNC (0.5%), PBA-BZ-COOH/MNC (1%), PBA-BZ-COOH/MNC (2%), and PBA-BZ-COOH/MNC (3%)

Coating samples	C_{dl} (μF cm^2)	R_p (Ω cm^2)	Q_{dl} (μΩ^{-1}s^n cm^2)	n	R_{ct} (kΩ cm^2)	η_1 (%)
Bare MS	——	——	1.238	0.77	0.354	——
PBA-BZ-COOH	0.01306	62.42	0.2728	0.52	4.375	91.91
PBA-BZ-COOH/MNC (0.5%)	0.01256	65.94	0.2656	0.52	4.753	92.55
PBA-BZ-COOH/MNC (1%)	0.01175	69.24	0.2559	0.51	5.018	92.95
PBA-BZ-COOH/MNC (2%)	0.01031	71.88	0.2326	0.54	5.297	93.32
PBA-BZ-COOH/MNC (3%)	0.00937	79.91	0.2313	0.55	5.552	93.62

where Y_o and ω_{max} are the *CPE* constant and an angular frequency, respectively. The n values are in the range from 0.51 to 0.52, suggesting that the circuit components behave as non-ideal capacitive.

The EIS corrosion protection efficiency (η_I) was determined using Eq. (6) [75].

$$\eta 1 = \frac{R_{ct} - R_{ct}^{\circ}}{R_{ct}} \tag{6}$$

where R_{ct} and R_{ct}° are the values of charge transfer resistance of coated MS and bare MS, respectively.

From Table 2, the R_{ct} values of MS significant increases from 0.354 kΩ cm^2 for bare MS to 4.357 kΩ cm^2 for the neat PBA-BZ-COOH coating and the highest value (5.552 KΩ cm^2) for PBA-BZ-COOH)/MNC (3%) composite coating. However, when the MNC content in the PBA-BZ-COOH matrix was increased, the R_{ct} values increases and the C_{dl} values significantly decreased, indicating that the formed protective film between substrate/electrolyte interfaces is improved with the MNC content increase [76, 77]. The plots of the impedance versus the frequency (Bode plots) and angle phase for the bare MS and Ms coated with PBA-BZ-COOH, PBA-BZ-COOH/MNC (1%), PBA-BZ-COOH/MNC (3%) are shown in Fig. S6. The impedance (Z_{real}) value is related to the resistance and the capacitance of the coating. From the Bode plot, it has been observed that the values of Z_{real} at low frequency (LF) of composites coatings were significantly increased after coated MS, compared with that of the bare MS, representing increases resistance of the coatings and decreases their capacitance, due to their had high ability against water and electrolytes. This result suggested that composites coatings could enhance the anti-corrosive performance of MS. Furthermore, from the phase angles plot, the variation of phase angles was seen clearly, which typically exposes the corrosion process of the specimens. Appeared peaks at high frequency indicate the protecting effect of the coatings, while that at intermediate frequency reveal that the coatings containing some micropores [69]. On the other hand, the phase angle of the bare MS just had one peak at the LF range, due to the occurrence of the corrosion process on its surface. The mechanism of anti-corrosive behavior of MS coated with PBA-BZ-COOH/MNC composites is shown in Fig. 15. Finally, the electrochemical Nyquist, Bode, and Tafel results confirm that the effectively dispersed MNC in the PBA-BZ-COOH matrix and the strong adhesion on MS substrates were led to the superior anti-corrosive behaviors of the nanocomposites coatings.

Adhesion test

The adhesion property of the neat PBA-BZ-COOH and its nanocomposite coatings on MS was evaluated by the cross-cut method [78], recorded by SEM analysis, as shown in Fig. S7. In general, each of the coatings did not show any peeling after the cross-cutting, indicating their strong adhesion to the MS substrate, which can be attributed to the conjugate of the PBZ matrix and the ability of COOH groups to form a strong hydrogen bonding with OH groups of the MS. The smoothness and adhesion of the cutting edge of the coatings are significantly enhanced with increasing the MNC contents in their nanocomposites, compared with the neat PBA-BZ-COOH coating. However, the diffusibility of the MNC and formation of Van der Waals interaction with MS substrate as well as the intercalated/exfoliated nanocomposite structure because of the formation of a physical interlocked structure with the substrate [79].

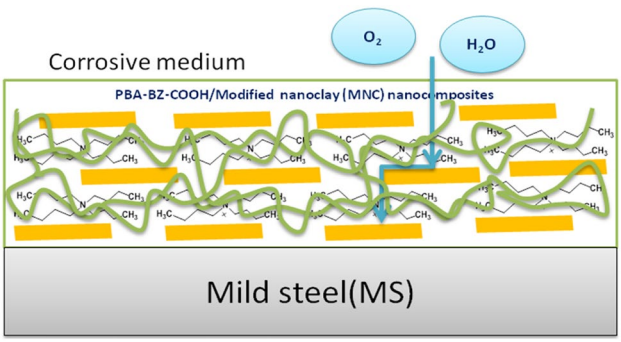

Fig. 15 Schematic cartoon for anti-Corrosion behavior mechanism of the MS coated with PBA-BZ-COOH/MNC composites

Conclusions

A novel benzoxazine monomer (BA-BZ-COOH) and its nanocomposites have been successfully prepared. The DSC analysis of BA-BZ-COOH showed a significantly lower polymerization temperature (167 °C) compared with the classical benzoxazine monomers due to the presence of the carboxylic acid group in the BA-BZ-COOH. The values of UV shielding of the PBA-BZ-COOH/MNC (3%) composite were about 97 and 85% at wavelength 275 and 375 nm, respectively. The electrochemical results revealed that the R_{ct} value was increased and the C_{dl} value was decreased of the MS coated with PBA-BZ-COOH when the content of MNC increased in composite coatings. Finally, the high anti-corrosive performance of PBA-BZ-COOH/MNC nanocomposite coatings can be attributed to the modified nanoclay which leads to improving the barrier properties by reducing the permeability of the coatings for oxygen and water species.

Supplementary information The online version contains supplementary material available at https://doi.org/10.1007/s10965-021-02657-0.

Acknowledgements This study was supported financially by the Science and Technology Development Fund (STDF, Egypt) (call 6/STDF Basic and Applied Research Grants (STDF-BARG)/Basic and Applied Research Grants) Project ID: 28930.

Declarations

Conflicts of interest There are no conflicts to declare.

References

1. Zhang S, Ran Q, Fu Q, Gu Y (2019) Thermal responsiveness of hydrogen bonding and dielectric property of polybenzoxazines with different Mannich bridge structures. Polymer 175:302–309
2. Mohamed MG, Hsu KC, Kuo SW (2015) Bifunctional polybenzoxazine nanocomposites containing photo-crosslinkable coumarin units and pyrene units capable of dispersing single-walled carbon nanotubes. Polym Chem 6:2423–2433
3. Mohamed MG, Kuo SW (2016) Polybenzoxazine/polyhedral oligomeric silsesquioxane (POSS) nanocomposites. Polymers 8:225
4. Mohamed MG, Chen TC, Kuo SW (2021) Solid-State Chemical Transformations to Enhance Gas Capture in Benzoxazine-Linked Conjugated Microporous Polymers. Macromolecules 54:5866–5877
5. Mohamed MG, Meng TS, Kuo SW (2021) Intrinsic water-soluble benzoxazine-functionalized cyclodextrin and its formation of inclusion complex with polymer. Polymer 226:123827
6. Mohamed MG, Tsai MY, Wang CF, Huang CF, Danko M, Dai L, Chen T, Kuo SW (2021) Multifunctional Polyhedral Oligomeric Silsesquioxane (POSS) Based Hybrid Porous Materials for CO_2 Uptake and Iodine Adsorption. Polymers 13:221
7. Huang CF, Chen WH, Aimi J, Huang YS, Venkatesan S, Chiang YW, Huang SH, Kuo SW, Chen T (2018) Synthesis of well-defined PCL-b-PnBA-b-PMMA ABC-type triblock copolymers: toward the construction of nanostructures in epoxy thermosets. Polym Chem 9:5644–5654
8. Huang YS, Hsueh HY, Aimi J, Chou LC, Lu YC, Kuo SW, Wang CC, Chen HY, Huang CG (2020) Effects of various Cu(0), Fe(0), and proanthocyanidin reducing agents on Fe(iii)-catalysed ATRP for the synthesis of PMMA block copolymers and their self-assembly behaviours. Polym Chem 11:5147–5155
9. Mohamed MG, Tsai MY, Su WC, EL-Mahdy AFM, Wang CF, Huang CF, Dai L, Chen T, Kuo SW (2020) Nitrogen-Doped microporous carbons derived from azobenzene and nitrile-functionalized polybenzoxazines for CO_2 uptake Mater. Today Commun. 24:101111
10. Mohamed MG, Jr ECA, Matsagar BM, Na JB, Yamauchi Y, Wu KCW, Kuo SW (2020) Construction Hierarchically Mesoporous/Microporous Materials Based on Block Copolymer and Covalent Organic Framework. J Taiwan Inst Chem Eng 112:180–192
11. Mohamed MG, Elsayed MH, Elewa AM, EL-Mahdy AFM, Yang CH, Mohammed AAK, Chou HH, Kuo SW (2021) Pyrene-containing conjugated organic microporous polymers for photocatalytic hydrogen evolution from water. Catal Sci Technol 11:2229–2241
12. Mohamed MG, Ahmed MMM, Du WT, Kuo SW (2021) Meso/Microporous Carbons from Conjugated Hyper-Crosslinked Polymers Based on Tetraphenylethene for High-Performance CO_2 Capture and Supercapacitor. Molecules 26:738
13. Tu CW, Tsai FC, Chang CJ, Yang CH, Kuo SW, Zhang J, Chen T, Huang CF (2019) Surface-Initiated Initiators for Continuous Activator Regeneration (SI ICAR) ATRP of MMA from 2,2,6,6–tetramethylpiperidine–1–oxy (TEMPO) Oxidized Cellulose Nanofibers for the Preparations of PMMA Nanocomposites. Polymers 11:1631
14. Mohamed MG, Lin RC, Tu JH, Lu FH, Hong JL, Jeong KU, Wang CF, Kuo SW (2015) Thermal property of an aggregation-induced emission fluorophore that forms metal–ligand complexes with Zn $(ClO_4)_2$ of salicylaldehyde azine-functionalized polybenzoxazine. RSC Adv 5:65635–65645
15. Ishida H, Allen DJ (2001) Gelation behavior of near-zero shrinkage polybenzoxazines. J appl Polym Sci 79:406–417
16. Lin CH, Chang SL, Shen TY, Shih YS, Lin HT, Wang CG (2012) Flexible polybenzoxazine thermosets with high glass transition temperatures and low surface free energies. Polym Chem 3:935–945
17. Mohamed MG, Kuo SW (2019) Functional polyimide/polyhedral oligomeric silsesquioxane nanocomposites. Polymers 2019:26
18. Qi H, Pan G, Yin L, Zhuang Y, Huang F, Du L (2009) Preparation and characterization of high char yield polybenzoxazine/polyarylacetylene blends for resin-transfer molding. J Appl Polym Sci 114:3026–3033
19. Lin RC, Mohamed MG, Kuo SW (2017) Benzoxazine/Triphenylamine-Based Dendrimers Prepared through Facile One-Pot Mannich Condensations. Macromol Rapid Commun 38:1700251
20. Mohamed MG, Hsiao CH, Hsu KC, Lu FH, Shih HK, Kuo SW (2015) Supramolecular functionalized polybenzoxazines from azobenzene carboxylic acid/azobenzene pyridine complexes: synthesis, surface properties, and specific interactions. RSC Adv 5:12763–12772
21. Samy MM, Mohamed MG, Kuo SW (2020) Directly synthesized nitrogen-and-oxygen–doped microporous carbons derived from a bio-derived polybenzoxazine exhibiting high-performance supercapacitance and CO_2 uptake. Euro. Polym. J. 138:109954
22. Wu JY, Mohamed MG, Kuo SW (2017) Directly synthesized nitrogen-doped microporous carbons from polybenzoxazine resins for carbon dioxide capture. Polym Chem 8:5481–5489
23. Kiskan B, Koz B, Yagci Y (2009) Synthesis and characterization of fluid 1, 3-benzoxazine monomers and their thermally activated curing. J Polym Sci A Polym Chem 47:6955–6961

24. Kudoh R, Sudo A, Endo T (2010) A highly reactive benzoxazine monomer, 1-(2-hydroxyethyl)-1, 3-benzoxazine: activation of benzoxazine by neighboring group participation of hydroxyl group. Macromolecules 43:1185–1187
25. Andreu R, Reina J, Ronda J (2008) Carboxylic acid-containing benzoxazines as efficient catalysts in the thermal polymerization of benzoxazines. J Polym Sci A Polym Chem 46:6091–6101
26. Li S, Zou T (2012) Synthesis, characterization of new carboxylic acid-containing benzoxazine and its cocuring behaviors with bisoxazoline. J Appl Polym Sci 123:922–928
27. Mohamed MG, Ebrahium SM, Hammam AS, Kuo SW, Aly KI (2020) Enhanced CO_2 capture in nitrogen-enriched microporous carbons derived from Polybenzoxazines containing azobenzene and carboxylic acid units. J Polym Res 27:197
28. Kumaresan I, Pichaimani P, Ellappan S, Paramasivam M (2018) Ceria doped mullite reinforced polybenzoxazine nanocomposites with improved UV-shielding and thermo-mechanical properties. Polym Compos 39:2073–2080
29. Kumar S, Hariharan A, Alagar M, Dinakaran K (2020) Low-k and UV shielding polybenzoxazine nanocomposites synthesised from quinoline amine and bio-silica. Compos. Interfaces. https://doi.org/10.1080/09276440.2020.1833594
30. Caldona EB, De Leon ACC, Thomas PG, Naylor DF III, Pajarito BB, Advincula RC (2017) Superhydrophobic rubber-modified polybenzoxazine/SiO_2 nanocomposite coating with anticorrosion, anti-ice, and superoleophilicity properties. Ind Eng Chem Res 56:1485–1497
31. Alhwaige AA, Ishida H, Qutubuddin S (2020) Chitosan/polybenzoxazine/clay mixed matrix composite aerogels: preparation, physical properties, and water absorbency. Appl Clay Sci 184:105403
32. Salahuddin N (2009) The effect of polyoxypropylene-montmorillonite intercalates on polymethylmethacrylate. Polym Compos 30:13–21
33. Cha J, Jun GH, Park JK, Kim JC, Ryu HJ, Hong SH (2017) Improvement of modulus, strength and fracture toughness of CNT/Epoxy nanocomposites through the functionalization of carbon nanotubes. Compos B Eng 129:169–179
34. Selvaraj V, Jayanthi K, Lakshmikandhan T, Alagar M (2015) Development of a polybenzoxazine/TSBA-15 composite from the renewable resource cardanol for low-k applications. RSC Adv 5:4889–48907
35. Liu P (2007) Polymer modified clay minerals: A review. Appl Clay Sci 38:64–76
36. Aly KI, Mohamed MG, Younis O, Mahross MH, Abdel-Hakim M, Sayed MM (2020) Salicylaldehyde azine-functionalized polybenzoxazine: synthesis, characterization, and its nanocomposites as coatings for inhibiting the mild steel corrosion. Prog Org Coat 138:105–385
37. Mohamed MG, Kuo SW, Mahdy A, Ghayd IM, Aly KI (2020) Bisbenzylidene cyclopentanone and cyclohexanone-functionalized polybenzoxazine nanocomposites: Synthesis, characterization, and use for corrosion protection on mild steel. Mater. Today Commun. 25:101418
38. Tiptipakorn S, Damrongsakkul S, Ando S, Hemvichian K, Rimdusit S (2007) Thermal degradation behaviors of polybenzoxazine and silicon-containing polyimide blends. Polym Degrad stab 92:1265–1278
39. Patil DM, Phalak GA, Mhaske S (2017) Enhancement of anticorrosive performances of cardanol based amine functional benzoxazine resin by copolymerizing with epoxy resins. Prog Org Coat 105:18–28
40. Zhou C, Lin J, Lu X, Xin Z (2016) Enhanced corrosion resistance of polybenzoxazine coatings by epoxy incorporation. RSC adv 6:28428–28434
41. Selvaraj V, Raghavarshini T, Alagar M (2020) Evaluation of thermo-mechanical, dielectric and corrosion resistant properties of cardanol benzoxazine-epoxy based hybrid composites: A very low temperature curing pre-polymer for high performance paint related applications. High Perform Polym 32:524–539
42. Phalak GA, Patil DM, Mhaske S (2017) Synthesis and characterization of thermally curable guaiacol based poly (benzoxazine-urethane) coating for corrosion protection on mild steel. Euro Polym J 88:93–108
43. Takeichi T, Zeidam R, Agag T (2002) Polybenzoxazine/clay hybrid nanocomposites: influence of preparation method on the curing behavior and properties of polybenzoxazines. Polymer 43:45–53
44. Mohamed MG, Kuo SW (2019) Functional silica and carbon nanocomposites based on polybenzoxazines. Macromol Chem Phys 220:1800306
45. Chen Q, Xu R, Yu D (2006) Multiwalled carbon nanotube/polybenzoxazine nanocomposites: preparation, characterization and properties. Polymer 47:7711–7719
46. Andronescu C, Garea SA, Voicu G, Vasile E, Iovu H (2012) Nanocomposites based on a new polybenzoxazine resin and MMT. U.P.B. Sci Bull Series B 74:69–76
47. Laatar F, Jayan M, Padmanabhan P, Romdhane MRB, Srasra E (2018) Unsaturated polyester-nanoclay nanocomposite coatings for effective corrosion protection of steel. J Coat Technol Res 15:293–301
48. Lin CH, Chen ZJ, Chen CH, Wang MW, Juang TY (2017) Synthesis of a bisbenzylideneacetone-containing benzoxazine and its photo-and thermally cured thermoset. ACS Omega 2:3432–3440
49. Aly K, Hussein M (2015) New polymer syntheses part: 58. synthesis, characterization and corrosion inhibitive properties of new thiazole based polyamides containing diarylidenecyclohexanone moiety. Chinese J Polym Sci 33:1–13
50. Mohamed MG, Kuo SW (2020) Crown ether-functionalized polybenzoxazine for metal ion adsorption. Macromolecules 53:2420–2429
51. Zhang X, Mohamed MG, Xin Z, Kuo SW (2020) A tetraphenylethylene-functionalized benzoxazine and copper (II) acetylacetonate form a high-performance polybenzoxazine. Polymer 201:122552
52. Ishida H, Froimowicz P (2017) Advanced and emerging polybenzoxazine science and technology Elsevier
53. Gilbert E, Taverna ME, Dieser MF, Morales G, Spontón M, Estenoz D (2018) Synthesis and characterization of new thermosetting polybenzoxazines with other functional groups in the network. J Polym Res 25:114
54. Mohamed MG, Hsu KC, Hong JL, Kuo SW (2016) Unexpected fluorescence from maleimide-containing polyhedral oligomeric silsesquioxanes: nanoparticle and sequence distribution analyses of polystyrene-based alternating copolymers. Polym Chem 7:135–145
55. Mohamed MG, Lu FH, Hong JL, Kuo SW (2015) Strong emission of 2,4,6-triphenylpyridine-functionalized polytyrosine and hydrogen-bonding interactions with poly(4-vinylpyridine). Polym Chem 6:6340–6350
56. Krishnan S, Arumugam H, Kuppan C, Goswami A, Chavali M, Muthukaruppan A (2017) Silane-functionalized polybenzoxazines: a superior corrosion resistant coating for steel plates. Mater Corros 68:1343–5134
57. Maroufkhani M, Katbab A, Zhang J (2018) Manipulation of the properties of PLA nanocomposites by controlling the distribution of nanoclay via varying the acrylonitrile content in NBR rubber. Polym Test 65:313–321
58. Motawie AM, Madany MM, El-Dakrory AZ, Osman HM, Ismail EA, Badr MM, El-Komy DA, Abulyazied DE (2014) Physicochemical characteristics of nano-organo bentonite prepared using different organo-modifiers. Egypt J Pet 23:331–338
59. Samy MM, Mohamed MG, Kuo SW (2020) Pyrene-functionalized tetraphenylethylene polybenzoxazine for dispersing single-walled carbon nanotubes and energy storage. Compos Sci Technol 199:108360

60. Jesuarockiam N, Jawaid M, Zainudin ES, Sultan MTBH, Yahaya R (2019) Enhanced thermal and dynamic mechanical properties of synthetic/natural hybrid composites with graphene nanoplateletes. Polymer 11:1085
61. Guo Y, Bao C, Song L, Yuan B, Hu Y (2011) In situ polymerization of graphene, graphite oxide, and functionalized graphite oxide into epoxy resin and comparison study of on-the-flame behavior. Ind Eng Chem Res 50:7772–7783
62. Zhang Y, Liu X, Zhan G, Zhuang Q, Zhang R, Qian J (2019) Study on the synergistic anticorrosion property of a fully bio-based polybenzoxazine copolymer resin. Euro Polym J 119:477–486
63. Zhou C, Lu X, Xin Z, Liu J, Zhang Y (2013) Hydrophobic benzoxazine-cured epoxy coatings for corrosion protection. Prog Org Coat 76:1178–1183
64. Aly KI, Abbady M, Mahgoub S, Hussein M (2009) New polymer syntheses, Part 44: Synthesis, characterization, and corrosion inhibition behavior of new polyurea derivatives based on diaryl ether in the polymers backbone. J Appl Polym Sci 112:620–628
65. Bakshi MI, Ahmad S (2020) In-situ synthesis of synergistically active ceria doped polypyrrole oleo-polyesteramide hybrid nanocomposite coatings: Corrosion protection and flame retardancy behaviour. Prog Org Coat 147:105778
66. Chang CH, Huang TC, Peng CW, Yeh TC, Lu HI, Hung WI, Weng CJ, Yang TI, Yeh JM (2012) Novel anticorrosion coatings prepared from polyaniline/graphene composites. Carbon 50:5044–5501
67. Zhou C, Lu X, Xin Z, Liu J, Zhang Y (2014) Polybenzoxazine/SiO_2 nanocomposite coatings for corrosion protection of mild steel. Corros Sci 80:269–275
68. Raju A, Lakshmi V, Prataap RV, Resmi V, Rajan T, Pavithran C, Prasad VS, Mohan S (2016) Adduct modified nano-clay mineral dispersed polystyrene nanocomposites as advanced corrosion resistance coatings for aluminum alloys. Appl Clay Sci 126:81–88
69. Zhang R, Lu X, Lou C, Zhou C, Xin Z (2019) Preparation of diamine-based polybenzoxazine coating for corrosion protection on mild steel. J Polym Res 26:29
70. Poorteman M, Renaud A, Escobar J, Dumas L, Bonnaud L, Dubois P, Olivier MG (2016) Thermal curing of para-phenylenediamine benzoxazine for barrier coating applications on 1050 aluminum alloys. Prog Org Coat 97:99–109
71. Salehzadeh D, Marashi P, Sadeghian Z (2020) Electrophoretic deposited Ni (OH) 2-YSZ and NiO-YSZ nanocomposite coatings, microstructural and electrochemical evaluation. Surf Coat Technol 381:125155
72. Zulkifli F, Yusof MSM, Isa M, Yabuki A, Nik WW (2017) Henna leaves extract as a corrosion inhibitor in acrylic resin coating. Prog Org Coat 105:310–319
73. Hegazy MA, Badawi AM, Abd El Rehim SS, Kamel WM (2013) Influence of copper nanoparticles capped by cationic surfactant as modifier for steel anti-corrosion paints. Egypt J Pet 22:549–556
74. Hegazy M, Abdallah M, Alfakeer M, Ahmed H (2018) Corrosion inhibition performance of a novel cationic surfactant for protection of carbon steel pipeline in acidic media. Int J Electrochem Sci 13:68240–76842
75. Hegazy M, Hefny M, Badawi A, Ahmed M (2013) Nanosilicon dioxide/o-phenylenediamine hybrid composite as a modifier for steel paints. Prog Org Coat 76:827–834
76. Aly KI, Mahdy A, Hegazy MA, Al-Muaikel NS, Kuo SW, Mohamed MG (2020) Corrosion Resistance of Mild Steel Coated with Phthalimide-Functionalized Polybenzoxazines. Coatings 10:1114
77. Shirehjini FT, Danaee I, Eskandari H, Zarei D (2016) Effect of nano clay on corrosion protection of zinc-rich epoxy coatings on steel 37. J Mater Sci Technol 32:1152–1160
78. Chang KC, Hsu C, Lu H, Ji W, Chang C, Li W, Chang CH, Li WY, Chuang TL, Yeh JM, Liu WR, Tsai MH (2014) Advanced anticorrosive coatings prepared from electroactive polyimide/graphene nanocomposites with synergistic effects of redox catalytic capability and gas barrier properties. Express Polym Lett 8:243–255
79. Tripathy DK, Sahoo BP (2017) Properties and Applications of Polymer Nanocomposites. Springer